www.advenergysustres.com

Flash Synthesis of High-Performance Sub-Micron Low-Disorder LiNi_xCo_yAl_zO₂ Cathode Single Crystals

Thomas E. Ashton,* Shutao Wang, Michael J. Johnson, Callum Chisnall, Matthew G. Tucker, Helen Playford, Alexander J. E. Rettie, Jiacheng Wang, Yang Xu, and Jawwad A. Darr*

A rapid solid-state flash heat and quench (FHQ) synthesis approach has been used to facilitate the rapid formation of layered NCA Li-ion cathodes with low structural defects. LiNi $_x$ Co $_y$ Al $_z$ O $_2$ (NCA) materials prepared by FHQ reveal impressive gravimetric capacity at C/10 and 10C discharge rates (195 and 150 mAh g $^{-1}$, respectively) after a few minutes of heating a co-precipitate mixture with LiOH, providing >95% reduction in energy needed for heat-treatment versus conventional solid state synthesis routes. Combined X-ray diffraction, neutron scattering with pair-distribution-function analysis, and X-ray absorption spectroscopy for a range of heat-treated samples are used to identify the point at which Ni $^{2+}$ -Li $^+$ antisite defects are minimized in these materials, which is critical to their electrochemical performance.

1. Introduction

To support and enable emerging electronic technologies, ever more challenging energy density and performance demands are required of electrical energy storage devices. Layered Li-ion cathodes based on LiCoO₂ (LCO) have currently set the commercial benchmark for high power. This has led to the development of high-nickel cathodes (typically ≥ 80 at% Ni), due to the demand for increased energy density, lower materials cost, and ethical issues surrounding cobalt mining.^[1] Incorporating Ni into the layered $R\overline{3}m$ structure leads to higher capacities (≈ 200 mAh g⁻¹) and relatively higher voltages (>4 V), especially in LiNiO₂.^[2] However,

elevated Ni content can lead to structural instability and rapid degradation through cation mixing of Li and Ni, low thermal stability, surface reactivity, and oxygen evolution. To alleviate these issues, supporting elements such as Mn in LiNi_xMn_yCo_zO₂ (NMC) and LiNi_xCo_yAl_zO₂ (NCA) have been incorporated. However, NCA and NMC are prone to paired antisite (PAS) defects that form during synthesis, which hamper electrode kinetics and structural stability.

In the α -NaFeO₂ structure, mobile Li layers are sandwiched between MO_6 slabs (M=Ni, Co, Al), and segregation of these two layers ensures good ionic mobility. However, PAS defects can occur by concur-

rent swapping of Ni and Li atoms in their respective sites. This is reportedly enabled by the similar ionic radii of Ni²⁺ (0.69 Å) and Li⁺ (0.76 Å) compared to other available elements ($\text{Co}^{3+}_{(\text{hs})} = 0.61$ Å, $\text{Al}^{3+} = 0.535$ Å), facilitated by disproportionation of Ni³⁺ in Jahn–Teller distorted of LiNiO₂ species, leading to a relatively low formation energy of Ni²⁺ antisite defects.^[4] In contrast, recent structural studies have suggested this cannot be the case as the formation energy is composition-dependent.^[5] Regardless, the presence of large amounts of PAS defects has previously shown to contribute to: i) lower Li diffusion rates, limiting performance especially at charge/discharge rates in a battery cell; ii) lower structural stability by seeding the formation of the electrochemically inert

T. E. Ashton
Institute for Materials Discovery
UCL
7 Sidings St, London E20 2AE, UK
E-mail: t.ashton@ucl.ac.uk

E-mail: j.a.darr@ucl.ac.uk

S. Wang, C. Chisnall, J. Wang, Y. Xu, J. A. Darr Department of Chemistry UCL 20 Gordon St, London WC1H 0AI, UK

The ORCID identification number(s) for the author(s) of this article can be found under https://doi.org/10.1002/aesr.202500149.

© 2025 The Author(s). Advanced Energy and Sustainability Research published by Wiley-VCH GmbH. This is an open access article under the terms of the Creative Commons Attribution License, which permits use, distribution and reproduction in any medium, provided the original work is properly cited.

DOI: 10.1002/aesr.202500149

M. J. Johnson, A. J. E. Rettie Electrochemical Innovation Lab Department of Chemical Engineering UCL 20 Gordon St, London WC1H 0AJ, UK

M. G. Tucker Neutron Scattering Division ORNL 1 Bethel Valley Road, Oak Ridge, TN 37830, USA

H. Playford Neutron and Muon Source ISIS Didcot, Oxford OX11 0QX, UK

2699412, 0, Downloaded from https://advanced.onlinelibrary.wiley.com/doi/10.1002/asr.202500149 by NICE, National Institute for Health and Care Excellence, Wiley Online Library on [23/09/2025]. See the Terms and Conditions (https://onlinelibrary.wiley.

onditions) on Wiley Online Library for rules of use; OA articles are governed by the applicable Creative Commons

rock-salt phase, especially at the material's surface, hampering lithium removal and insertion. [6] As a result, different approaches have been explored to minimize PAS defects during synthesis: i) optimization of stoichiometry, [7] ii) inclusion of dopants, [8] and iii) thermal annealing. [9]

Generally, reducing the availability of Ni in NMC cathodes tends to reduce the concentration of PAS defects due to a shift in the Ni $^{3+}_{3a} \rightleftharpoons \text{Ni}^{2+}_{3b}$ equilibrium; however, this also reduces the energy density. [7] However, computational studies on isostructural $\text{LiNi}_x \text{Mn}_y \text{Co}_z \text{O}_2$ found that replacing Ni with Mn $^{4+}$ increases the concentration of PAS defects. [5] Therefore, in NCA (and other nickel-rich cathodes), the metal content is typically $\ge \! 80\%$ Ni.

Controlling the time and temperature (i.e., the thermodynamics) of any solid-state lithiation synthesis is the simplest way of minimizing PAS defects. Typically, synthesis of NCA and its analogs is carried out at elevated temperatures (>800 °C) in the time range 6–12 h, with slow ramp rates (\approx 5 °C min⁻¹), and sometimes requiring multiple steps. [10] Conventional theory dictates that PAS defects can be 'ironed out' after extended heattreatment durations, allowing elements to diffuse and locate sites to form a low-defect structure. However, recent work carried out on LiNiO2 cathodes has shown heat-treatment times can be shortened to a total time of \approx 3.6 h by using an intimately mixed coprecipitate precursor to minimize diffusion distances, and accelerate structural consolidation and PAS defect minimization.[11] As heat-treatment is still the most energy-intensive step of current NCA syntheses, these timescales need to be reduced to lower manufacturing costs for industry and also to help accelerate materials discovery research.

Recent studies have suggested that other approaches to heattreatment can indeed provide routes to phase pure materials at extremely low timescales (in as little as 1.5 s), such as rapid resistive joule heating methods, which also report improved electrochemical performance.^[12–14] However, as these routes rely on resistive heating, thermal transfer is critically limited at larger sample volumes. Herein, we describe a rapid bottom-up solidstate route to low PAS defect NCA single crystals using a scalable, convection-based flash heat and Quench (FHQ) methodology.

2. Results and Discussion

The obtained powders were brown in color after co-precipitation, changing to black free-flowing powders after mixing with LiOH, FHQ, and subsequent gentle hand grinding.

2.1. High-Throughput Materials Optimization of FHQ-NCA

Powder X-ray diffraction (PXRD) patterns were collected for all 100 FHQ-NCA samples, with an $R\overline{3}m$ structure typical of NCA identified in all cases (**Figure 1a**). The $I_{(003)}/I_{(104)}$ (peak) ratio, which has previously been used to qualitatively estimate the extent of ${\rm Li^+}_{3a}/{\rm Ni^{2+}}_{3b}$ antisite mixing, was calculated for each sample (Figure 1b). Literature reports concerning the $I_{(003)}/I_{(104)}$ ratio suggest that a value of close to 1.2 for similar high Ni content structures (e.g., NMCs) is an indication of a well-crystallized $R\overline{3}m$ structure with minimal defects. Therefore, there is a strong correlation with reduced defects and excellent electrochemical performance. [16]

Under the FHQ conditions explored, the $I_{(003)}/I_{(104)}$ ratio from PXRD peak data was largest in the heat-treatment time range 2–40 min and the temperature range 825–900 °C. The maximum $I_{(003)}/I_{(104)}$ ratio of 1.07 (suggesting low structural defects) was found to be for the sample heat-treated at 850 °C for 10 min (sample NCA_850_10), which was a significantly short time compared to the battery cathode synthesis literature. Moving away from these optimized conditions resulted in lower $I_{(003)}/I_{(104)}$ ratio values, suggesting an increasingly defective structure. At lower temperatures and shorter heat-treatment times, a lower $I_{(003)}/I_{(104)}$ ratio was likely due to the formation of defects from insufficient energy to properly crystallize the

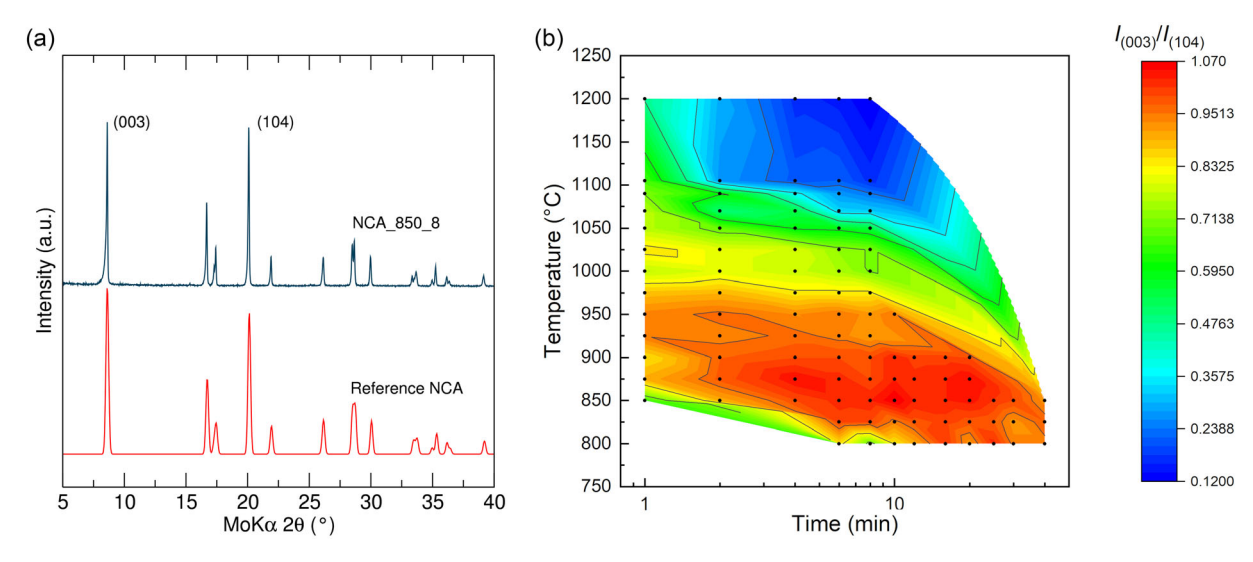


Figure 1. a) PXRD pattern showing a single-phase structure typical of NCA compared to a reference sample (inorganic crystal structure database coll. code: 257 247). b) Interpolated heat map of the $I_{(003)}/I_{(104)}$ peak intensity ratio estimated from PXRD with respect to heat-treatment time and temperature for 100 FHQ-NCA samples. The linear interpolation is estimated from the observed values (black dots) and provided as a guide to the eye.

on Wiley Online Library for rules of use; OA articles are governed by the applicable Creative Commons

www.advenergysustres.com

structure. At higher temperatures and longer FHQ times, the lower $I_{(003)}/I_{(104)}$ ratios were thought to arise from defects due to crystals sintering or Li volatilization [the latter would result in a Li deficiency and vacancies (v_{Li}) in the final structure]. However, preceding studies have shown that increasing $v_{I,i}$ in analogous $R\overline{3}m$ Li MO_2 structures leads to an increase in the $I_{(003)}/I_{(104)}$ ratio.^[17] Therefore, the decrease in the $I_{(003)}/I_{(104)}$ $I_{(104)}$ ratio with increasing temperature and/or time appears unprecedented: prevailing literature on LiMO2 has suggested that defects can be minimized by increasing heat-treatment duration or temperature. [18] To explore this further, longduration control experiments were carried out on the same precursors for 12 h at 800 and 850 °C (sample LD-NCA_800 and LD-NCA_850, respectively), giving $I_{(003)}/I_{(104)}$ ratios of 1.02 and 0.92, respectively. Thus, the observed narrow "window of opportunity" where there is a maximum $I_{(003)}/I_{(104)}$ ratio has been facilitated by the FHQ method that allows rapid quenching when the sample is removed from the hot furnace, effectively "locking in" the structure or state of the material at that point.

2.2. Electrochemical Characterization

To establish structure property relationships of the FHQ-NCA cathodes, all the samples heat-treated at 850, 875, and 900 °C were prepared and tested as Li-ion half cells by galvanostatic cycling with potential limitation (GCPL). GCPL was carried out from 2.7 to 4.3 V at increasing charge and discharge rates of C/10, C/5, 1C, 5C, and 10C (1C = 190 mA g^{-1}). Figure 2 shows a heat-map with linear interpolation for the gravimetric discharge capacity (QDischarge) observed during GCPL at C/10 (Figure 2a), 1C (Figure 2b), and 10C (Figure 2c). Q_{Discharge} lowered with increasing charge/discharge rate for all samples due to the kinetic limitations of charge transport. Increasing temperature or decreasing time of the synthesis typically led to a decrease in Q_{Discharge}, with the trend becoming clearer with increasing C-rate. FHQ-NCA samples prepared at 850 °C for 8 min (NCA_850_8) and 10 min (NCA_850_10) gave the highest gravimetric capacities at all C-rates, e.g., for sample (NCA_850_8), the capacity values were 196, 174, and 123 mAh g⁻¹ at C/10, 1C, and 10C, respectively. Similarly, for sample (NCA_850_10) where the

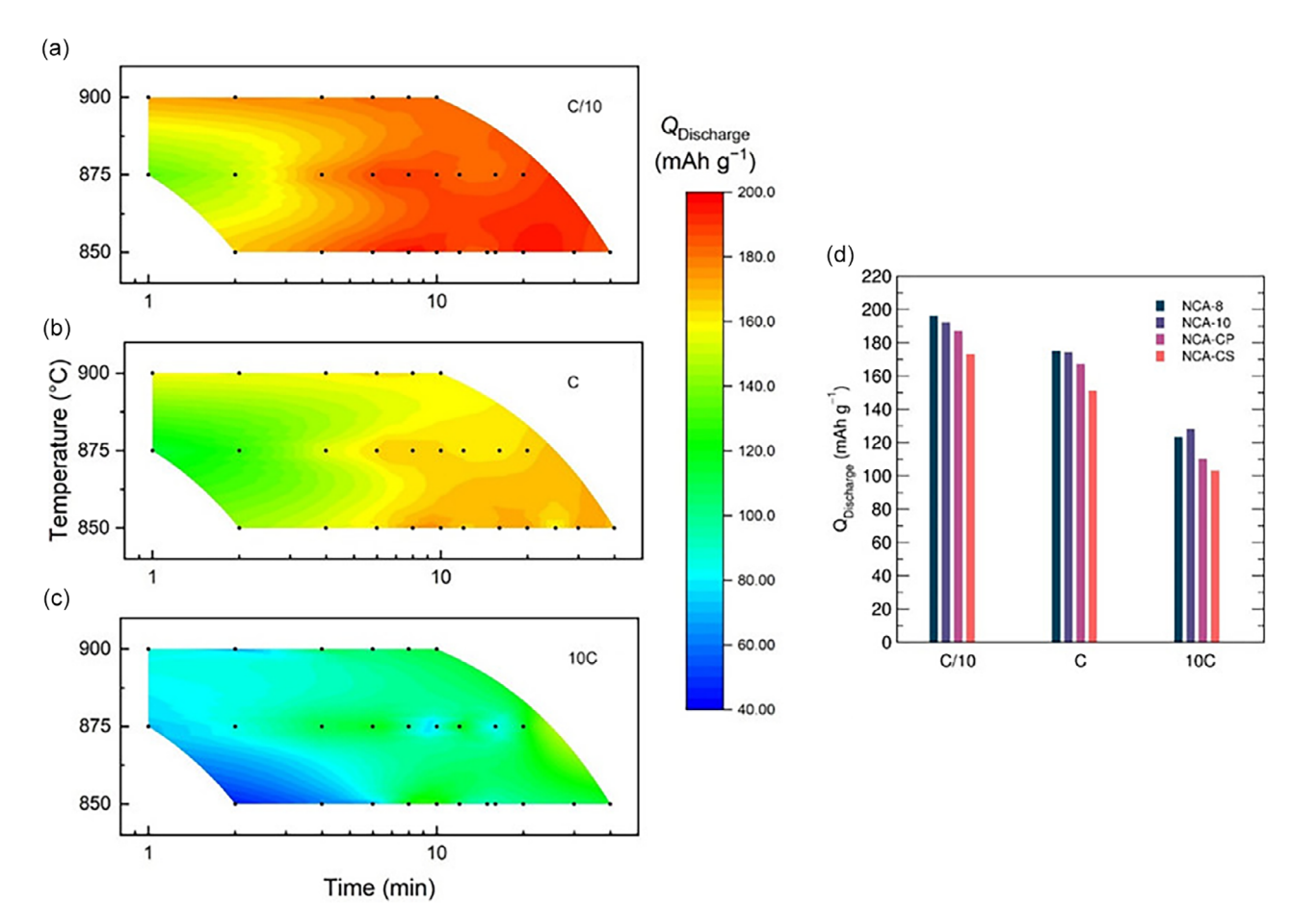


Figure 2. Interpolated heat map of gravimetric capacity for FHQ-NCA versus heat treatment time and temperature, carried out cycling rates of a) C10, b) 1C, and c) 10C. The linear interpolation is estimated from the observed values (black dots) and provided as a guide to the eye. d) Average discharge capacity observed for the NCA samples prepared at 850 °C for 8 and 10 min versus commercial Targray NCA (NCA-CP) and commercial cathode sheet (NCA-CS).

2699412, 0, Downloaded from https://advanced.onlinelibrary.wiley.com/doi/10.1002/asr.202500149 by NICE, National Institute for Health and Care Excellence, Wiley Online Library on [23/09/2025]. See the Terms and Conditions (https://onlinelibrary.wiley.

Wiley Online Library for rules of use; OA articles are governed by the applicable Creative Commons

www.advancedsciencenews.com

capacity values were 192, 174, and 128 mAh $\rm g^{-1}$ at C/10, 1C, and 10C, respectively.

A summary of these capacities is shown in Figure 2d and compares favorably with identical tests carried out on NCA commercial powders (NCA-CP), where the capacity values were 187, 167, and 110 mAh g $^{-1}$ at C/10, 1C, and 10C, respectively. Preprepared commercial sheets (NCA-CS) revealed capacity values of 173, 151, and 103 mAh g $^{-1}$ at C/10, 1C, and 10C, respectively. Cycling data for all commercial NCA samples are given in Supporting Information Figure S1. Most notably, the high-rate performance of FHQ-NCA at 10C has superior performance to comparable commercial NCA.

To assess the stability of the best cathode materials, long-term electrochemical cycling was carried out (850 °C for 8 and 10 min samples). **Figure 3**a shows the gravimetric capacity over 100 cycles at 1C (0.19 A g $^{-1}$). While both samples showed similar initial capacities of 195 mAh g $^{-1}$ (8 min sample) and 197 mAh g $^{-1}$ (10 min sample), the 8 min FHQ-NCA sample showed a better capacity retention (84%) compared to the 10 min sample (79%). Figure 3a also shows the gravimetric capacities for these samples over 150 cycles at 10C (1.9 A g $^{-1}$). Again, both showed similar initial capacities of 126 and 132 mAh g $^{-1}$ (sample NCA_850_8 and NCA_850_10, respectively) and similar capacity retentions (67% and 64%, respectively).

Cycling profiles (Figure 3b) were used to further investigate FHQ-TNCA at 1C, showing a typical discharge profile for NCA with an average operating voltage around 3.75 V. Although there is an apparent capacity loss over 100 cycles, the general redox behavior is preserved. However, a sequentially larger drop in potential is observed with increased cycle number. Additionally, a simultaneous loss of distinct plateaus for individual Ni and Co redox is observed after 10 cycles.

2.3. Structural Study of FHQ-NCA

To investigate the structural evolution of defects with increasing heat-treatment duration, neutron powder diffraction (NPD) was carried out on samples prepared at 800 °C for 4, 6, 8, 10, and 12 min. Figure 4a shows the Rietveld refinement fits to the time-of-flight data; a reasonable fit was obtained for all samples using three phases: i) an $R\overline{3}m$ structured layered NCA phase $(R\overline{3}m')$, ii) a second $R\overline{3}m$ phase $(R\overline{3}m')$, and iii) an Li_2CO_3 impurity phase. For both $R\overline{3}m$ phases, a $(\text{Li}_{1-\delta}\text{Ni}_{\delta})_{3b}(\text{Li}_{\gamma}\text{Ni}_{z-\gamma}\text{Co}_{\gamma}\text{Al}_{z})_{3a}\text{O}_{2}$ model was employed to account for $\text{Li}^+\text{-Ni}^{2+}$ cationic disorder (δ) similar to the author's previous work on analogous structures. [17] A summary of the values obtained from the Rietveld refinement is given in Table S1, Supporting Information.

The $R\overline{3}m'$ phase was found to be significantly more abundant (>75%, Figure 4b) and less disordered (Figure 4c) than $R\overline{3}m''$ in all samples. As heat-treatment time was increased, the amount of $R\overline{3}m'$ also increased with the concurrent consumption of $R\overline{3}m''$ and the LiOH source (manifested as a diminishing Li₂CO₃ fraction). This suggested a direct relationship between defect concentration and Li incorporation. Interestingly, although a continual reduction in the average defect concentration was observed, a sharp minimum at 8 min (δ = 2.7%) was revealed in the material along with the best capacity retention (NCA_850_8), in good agreement with the initial PXRD screening data.

To further elucidate structural relationships, neutron pair-distribution-function (N-PDF) analysis was carried out on the five NCA samples heat-treated at 850 °C in the time range 4 to 12 min. The N-PDF transforms (**Figure 5**a) showed a good fit to the (Li_{1- δ}Ni_{δ})_{3 δ}(Li_{γ}Ni_{δ - γ}Co_{γ}Al_{δ})_{3 δ}O_{δ} model applied. Figure 5b shows the extracted occupancy values for each element contributing to the PAS defects (Ni_{3 δ} and Li_{3 δ}). Although the magnitude of the occupancies is lower, and Ni²⁺-Li⁺ mixing is nonstoichiometric with Li_{3 δ} values consistently lower than Ni_{3 δ}, the Ni_{3 δ}, and Li_{3 δ} occupancies from N-DPF follow a broadly similar trend to the weighted average defects from NPD, with minimization at 8 min for Ni_{3 δ} (\approx 2.55%) and 10 min for Li_{3 δ} (\approx 0.65%). This may suggest that the minimization of Ni_{3 δ} defects in NCA is more critical to electrochemical performance than Li_{3 δ}, but further work would be needed to clarify this.

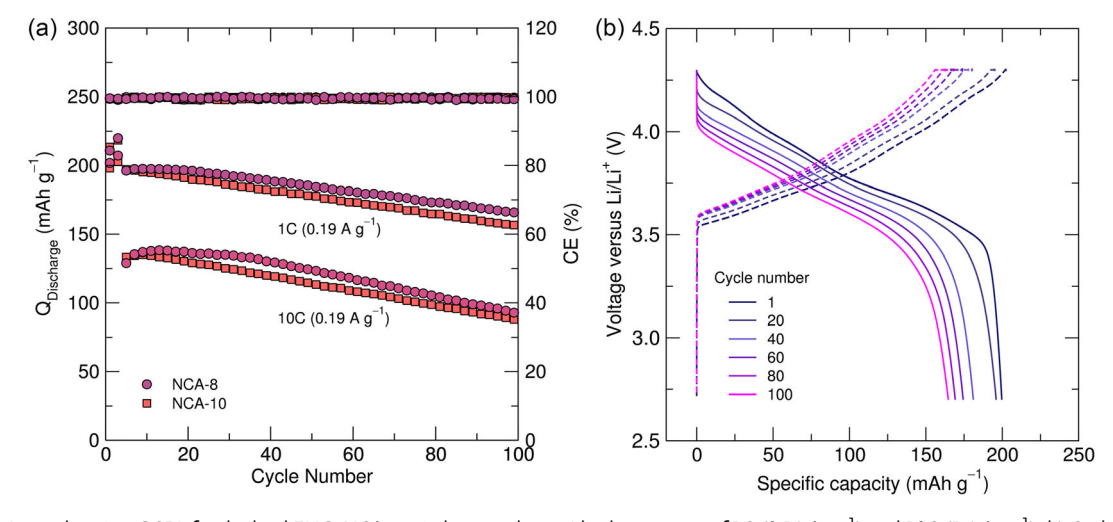


Figure 3. a) Long-duration GCPL for the lead FHQ-NCA carried out at charge/discharge rates of 1C (0.19 A g^{-1}) and 10C (1.9 A g^{-1}). b) Cycling profiles at 1C for NCA prepared at 850 °C for 8 min.

for Health and Care Excellence, Wiley Online Library

on [23/09/2025]. See the Term:

nditions) on Wiley Online Library for rules of use; OA articles are governed by the applicable Creative Commons

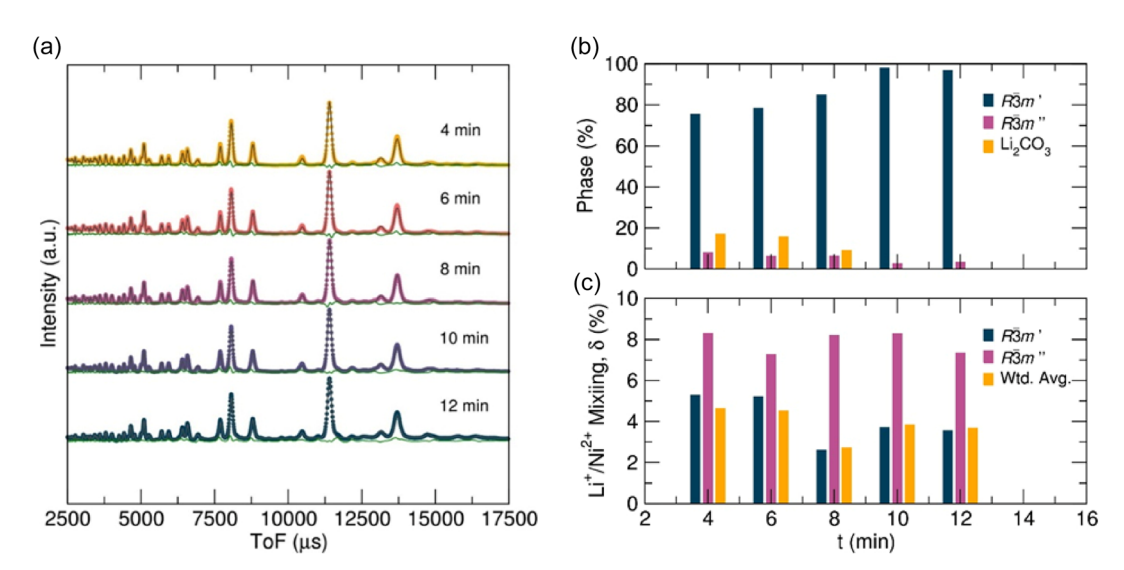


Figure 4. a) Rietveld refinement of NPD data for FHQ-NCA prepared at 850 °C in the time range 4–10 min. b) Phase percentage and c) lithium-nickel cation disorder (δ) estimated from Rietveld refinement. The average δ values are weighted against the phase %.

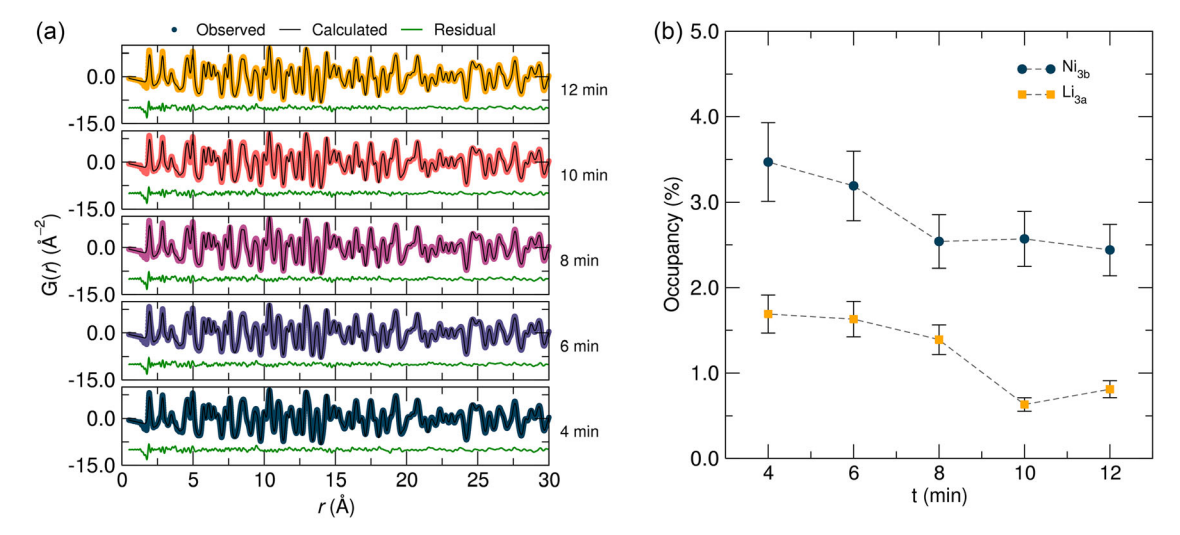


Figure 5. a) N-PDF data for NCA heat-treated at 850 °C for 4 to 12 min. b) Extracted antisite occupancy values from the PDF fitting.

2.4. Electronic Properties of FHQ-NCA Cathode Materials

To better understand the location of the two discrete $R\overline{3}m$ phases identified by NPD, bulk and surface electronic properties were investigated using X-ray absorption spectroscopy (XAS) and X-ray Photoelectron Spectroscopy (XPS), respectively. XAS was performed on five FHQ-NCA samples to assess any changes in: (i) oxidation state changes from the X-ray absorption near-edge structure (XANES), and (ii) local structure changes from the Extended X-ray absorption fine structure (EXAFS). The Co-K edge (Figure 6a) and Ni-K edge (Figure 6b) XANES spectra for each of the samples heat-treated for 4 to 12 min. A weak preedge feature is observed in all cases (centered on \approx 7711 eV for Co and \approx 8320 eV for Ni) arising from the dipole allowed transition of a core 1s electron to an asymmetric 3 d electronic state,

suggesting the departure of the metal atoms' environment from a perfect octahedral state (tetrahedralization). For Ni, this is reportedly caused by hybridization of Ni 4p electrons with the nearest O 2p electrons, and attributed to Ni²+ occupying a Li site in good agreement with the structural observations. [19] The rising edge (1s to np transitions) in the range ≈ 8341 to 8352 eV was indicative of the oxidation state. For all samples, there was no significant change in the oxidation state, confirming the low concentration of Ni²+ within each sample. Previous combined experimental and computational XANES studies have also shown that the stepped profile in the Ni-K XANES rising edge arose from a >50% Li occupancy. [19]

The EXAFS spectra collected for the five FHQ-NCA samples (Figure 6c,d) showed similar relationships: two primary features at \approx 1.5 and \approx 2.5 Å corresponded to the first shell metal–oxygen

for Health and Care Excellence, Wiley Online Library

onditions) on Wiley Online Library for rules of use; OA articles are governed by the applicable Creative Commons

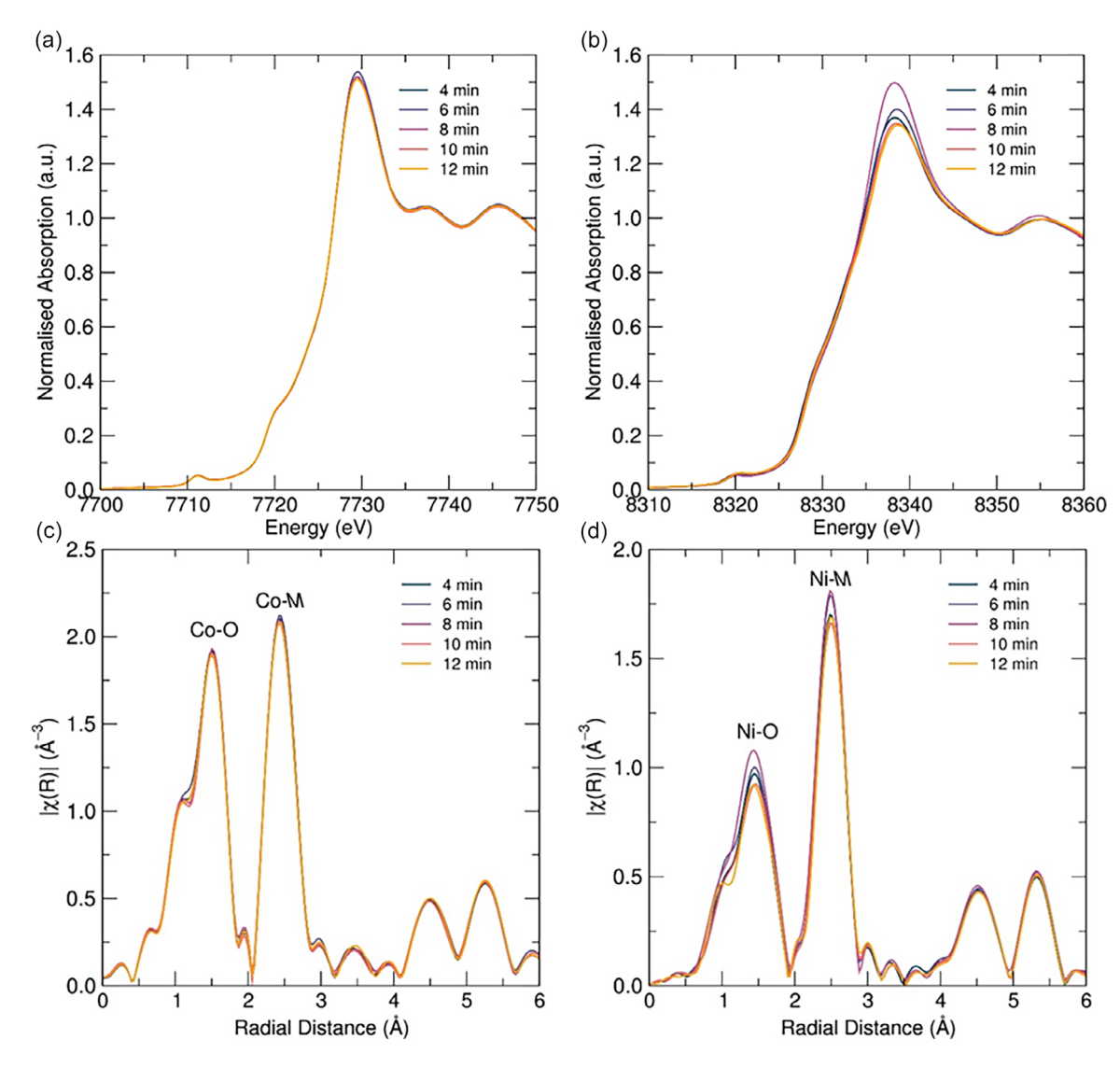


Figure 6. XANES spectra for a) Co K-edge and b) Ni K-edge for FHQ-NCA prepared at 850 °C for 4 to 12 min. EXAFS spectra for c) Co K-edge and d) Ni K-edge for FHQ-NCA prepared at 850 °C for 4 to 12 min.

and second shell metal–metal distances in the layered structure, respectively. In agreement with the XANES, there was no significant contribution from a first shell metal-metal interaction in the Ni K-edge EXAFS (Figure 6d), supporting the conclusion of a low bulk Ni²⁺ concentration (<5%).

In contrast, **Figure 7**a shows the Ni 2p XPS data for the FHQ-NCA samples and the untreated NCA precursor. Fitting the Ni 2p edge data, the main features located at 861 eV (Ni $2p_{1/2}$) and 854 eV (Ni $2p_{3/2}$) showed contributions for both Ni³⁺ and Ni²⁺. Ni³⁺ percentages were estimated by fitting these contributions and are shown in Figure 7b. Prior to heat-treatment, the Ni atoms exist largely in the 2+ state (ca. 79%) at the material's surface. Upon heat-treatment, the amount of Ni²⁺ begins to decrease with a minimum amount at 8 min (44%), subsequently rising again and becoming greater than the initial precursor at 12 min (88%). The Ni²⁺ concentrations in samples contrast with the observations of the XAS results. Due to the short inelastic

mean free path of photoelectrons for the core levels (in the range 5–25 Å), XAS has limited penetration, i.e., surface sensitivity, and suggests that the majority of Ni^{2+} present in each sample was primarily located at the materials' surface. [20]

2.5. Microstructure of FHQ-NCA Particles

Scanning Electron Microscopy (SEM) was performed to investigate the microstructure of sample NCA_850_10 (Figure 8). Although some larger agglomerates were identified, the sample typically showed well-defined primary octahedral-shaped crystals with a mean diameter of $\overline{x}=248\pm 5$ nm ($\sigma=43\pm 5$ nm). The impact of crystallinity (with single crystal particles at the extreme end) has previously been discussed in the literature, suggesting that increased crystallinity directly leads to improved performance due to enhanced structural stability in NCA cathodes. ^[21] This may be a contributing factor to the impressive performance

26999412, 0, Downloaded from https://advanced.onlinelibrary.wiley.com/doi/10.1002/æsr.202500149 by NICE, National Institute for Health and Care Excellence, Wiley Online Library on [23/09/2025]. See the Terms

on Wiley Online Library for rules of use; OA articles are governed by the applicable Creative Commons

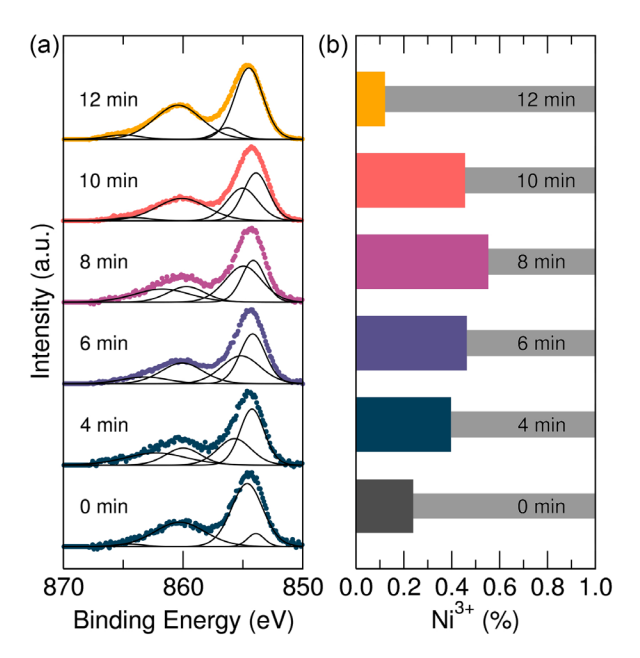


Figure 7. a) XPS of the Ni 2p edge for FHQ-NCA samples prepared at 850 °C in the range 0 to 12 min. b) Fraction of Ni³⁺ detected by XPS (vs. overall Ni³⁺+Ni²⁺ content).

of the FHQ sample NCA_850_10, supported by the sharp reflections observed in the XRD patterns. Furthermore, it is highly likely that the average size of the particles also contributes to the excellent rate performance of our NCA compared to the commercial standard (with multimicron particles^[22]), allowing faster diffusion kinetics at the particle interface.^[23]

2.6. Proposed Mechanism for FHQ Synthesis of Submicron NCA

Figure 9a shows the heating profiles for the reactions monitored using thermocouples during the heat treatment process. As expected, there is a rapid increase in temperature, with the

precursors reaching the maximum temperature (850 °C) in 230 s (3.8 min) after the initial 1 min for the introduction of the crucible to avoid thermal shock. Upon removal of the samples, rapid cooling occurs, reaching <200 °C in 160 s. Integrating the area under each curve (Figure 9b) shows a linear increase in thermal energy applied to each sample with increasing time, arbitrarily defined here as Kelvin seconds (K·s). Thus, the pure application of thermal energy cannot alone account for the nonlinear relationship between synthesis conditions and the defect concentrations observed.

The facile synthesis reported herein was possible due to the mixed precursor being in the form of an intimate submicron mixture of the multimetallic metal oxide/hydroxides and Li hydroxide. Compared to conventional solid state synthesis, i) minimizing the size of the reactants and ii) ensuring enhanced elemental homogeneity are critical to accelerating the rate of reaction. This was facilitated by using rapid hydrothermal precipitation of the metallic elements and adding a lithium source by incipient wetness shown in Figure 10a. When the intimate precursor mixture was introduced into a preheated furnace, the radiated heat was sufficient to drive the solid-state reaction on the surface to form the layered oxide, and Ni2+3a defects formed to stabilize the structure. Concurrently, the large amount of Li⁺ at the surface reduced Ni atoms to the 2+ state (from charge balance), leading to bifurcation of the $R\overline{3}m$ structure to $R\overline{3}m'$ and a surface layer of $R\overline{3}m''$ in the first few minutes. As the heating continued (Figure 10b), more LiOH was consumed, converting $R\overline{3}m''$ to $R\overline{3}m'$. Samples that were then removed from the hot furnace (quenching) at the precise point when all LiOH had just about been consumed were found to contain the lowest defects overall and enhanced electrochemical properties. Before this time, any LiOH that had not been consumed was visible as it formed Li₂CO₃.

2.7. Scale-up of FHQ-NCA

Enabling rapid heat treatments through the use of these tailored precursors potentially provides a new avenue for industrial cathode production, with significantly lower energy costs. Whereas

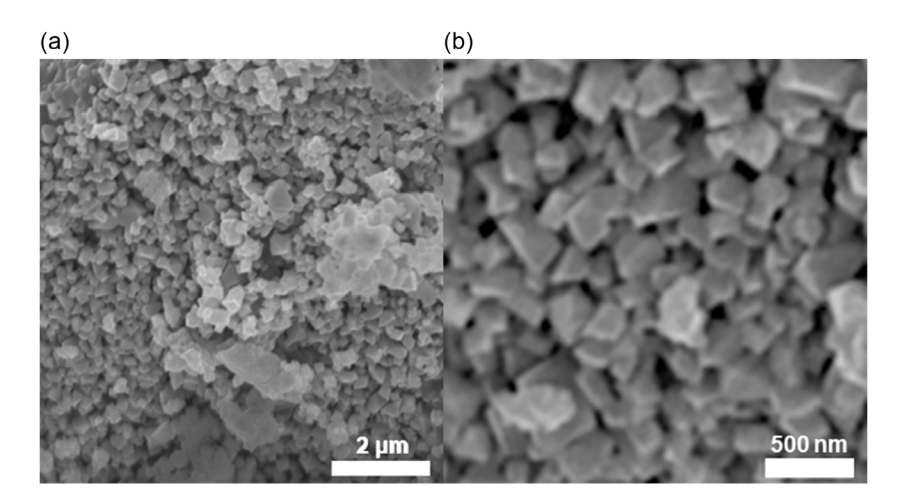


Figure 8. Scanning electron micrograph of a) NCA prepared by FHQ at 850 °C for 8 min and b) magnified image showing highly faceted octahedral single crystals of NCA.

26999412, 0, Downloaded from https://advanced.onlinelibrary.wiley.com/doi/10.1002/aesr.202500149 by NICE, National Institute for Health and Care Excellence, Wiley Online Library on [23/09/2025]. See the Term

onditions) on Wiley Online Library for rules of use; OA articles are governed by the applicable Creative Commons

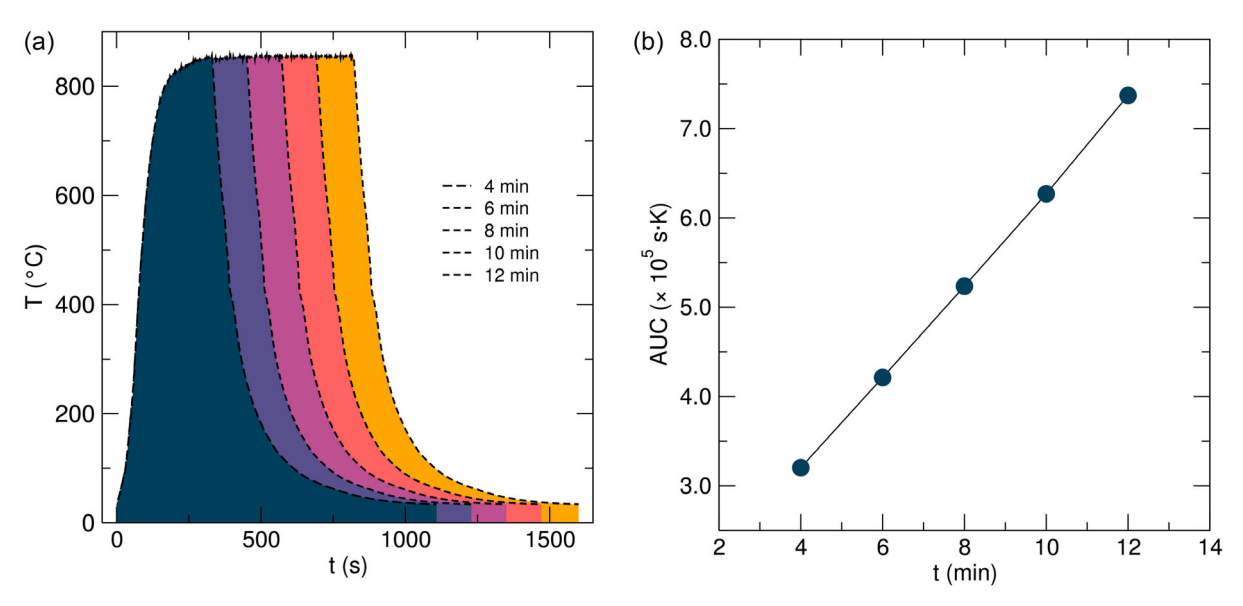


Figure 9. a) Heating profiles for NCA samples heated at a nominal 850 °C for 4 min to 12 min. b) Area under the curve approximating the integral using the trapezoid rule for each heating profile showing a linear relationship ($R^2 = 0.9999$).

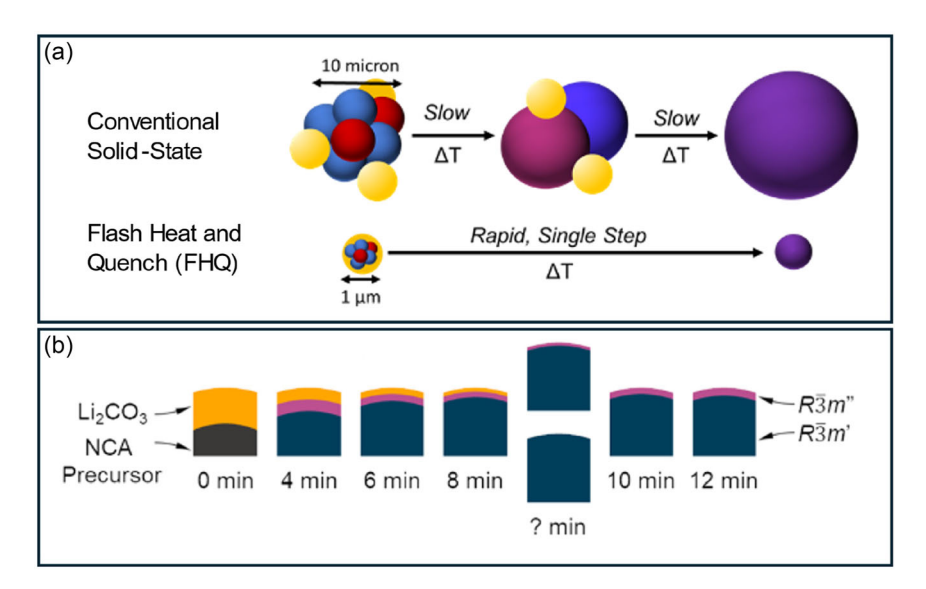


Figure 10. a) Schematic showing the advantages of the nanoprecursor FHQ approach versus conventional multistep solid-state. The lithium source is shown in yellow, and the constituent metal-containing precursors in blue and red. b) Schematic of the proposed phase formation showing the transformation from the lithiated precursor to the two-phase R3m system with a defect-rich surface.

commonly employed stirred tank reactions require long durations exceeding 20 h, this process enables continuous production of the precursors at the 500 g/h scale by the green hydrothermal route described here, and demonstrated in previous publications. [24] Furthermore, typical scaling of solid-state heat treatments can suffer from poor thermal transfer of the bulk precursor, limiting the rate of reaction. However, the authors have explored the feasibility of scaling up to 80 g shown in Figure 11, suggesting that heat transfer issues are limited in comparison to joule heating methods.

As shown in Figure 11a, four concurrent batches of 20 g of NCA (80 g total) showed identical structure, with a calculated I(003)/I(104) ratio of 1.05, in excellent agreement with the optimal 8 and 10 min NCA. The resulting electrochemical performance (Figure 11b) showed similar behavior to the smaller batches, with a capacity of 123 mAh g⁻¹ at 10C and outstanding capacity retention of 98% at C/10 after 120 cycles. Thus, the short duration of the FHQ process demonstrated herein may feasibly be translated to continuous heat treatment methodologies (such as belt-driven furnaces).

onlinelibrary.wiley.com/doi/10.1002/aesr.202500149 by NICE, National Institute

and Care Excellence, Wiley Online Library on [23/09/2025]. See the Terms

ons) on Wiley Online Library for rules of use; OA articles are governed by the applicable Creative Commons

www.advenergysustres.com

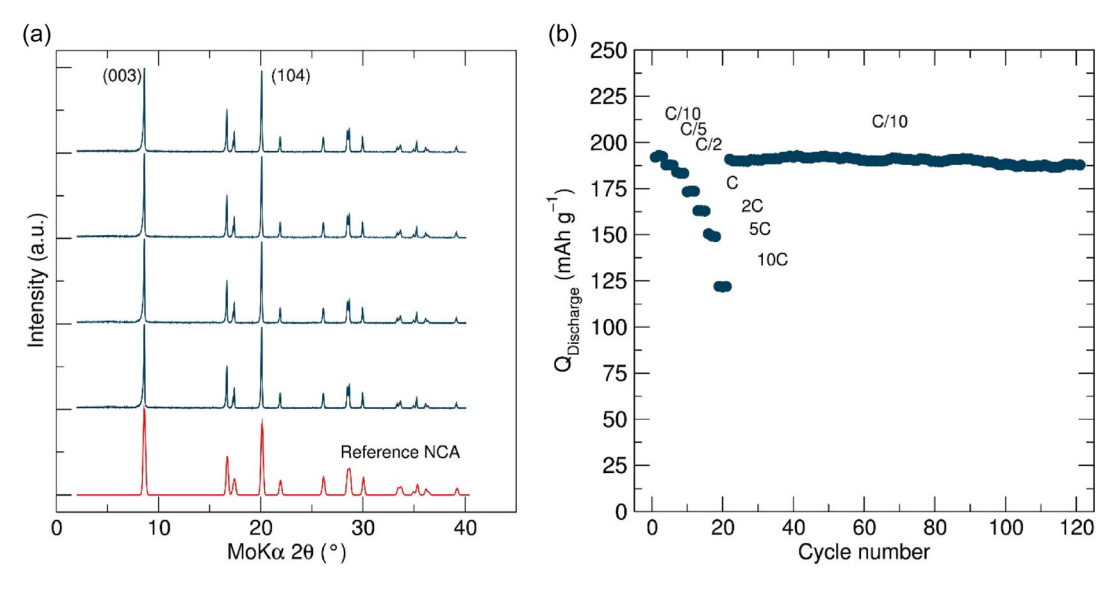


Figure 11. a) PXRD patterns collected for four concurrent batches of NCA totaling 80 g. b) The performance during constant current constant voltage galvanostatic cycling of the resulting scaled-up NCA after homogenization of the four batches at various charge/discharge rates.

3. Conclusions

The use of intimately mixed (submicron level) precursors with lithium hydroxide was shown to provide a rapid pathway to the direct and seamless synthesis of low-defect NCA cathodes with no grinding whatsoever. This precursor mixture ensured that diffusion distances were relatively short, enabling an efficient and complete solid-state reaction via the FHQ process in only a few minutes. This is in comparison to more conventional solid-state reactions, where larger precursor particles (with a lower degree of intimacy of the respective elements) would require multiple grinding and heating steps to create new interfaces where diffusion/reactions can occur.

Furthermore, the FHQ process was also able to produce submicron cathode crystals that may have contributed to improved performance, rather than typical micron-sized particles. Other potential benefits of the rapid heating (compared to slow ramping) might have been the direct reaction of 'more reactive' LiOH with the precursors, rather than a less reactive Li₂CO₃ intermediate, lowering the energy barrier to forming the ordered $R\overline{3}m$ phase.

In closing, quenching of the sample by removal from the hot furnace (at the optimum conditions) made it possible to "lock in" and capture the low defect state that also coincided with the point at which the last of the Li source had been used up. Thereafter, if the NCA was left in the furnace for longer times, the number of PAS defects was seen to increase, that most likely would include the effects of particles sintering and coarsening. This has also been confirmed by the differences in bulk and surface chemistry by complementary XRD, XPS, XAS, EXAFS, NPD, and N-PDF analyzes, with the majority of Ni²⁺ located at the particles' surface and the minimization of the surface phase and defect concentration at the critical time. The FHQ methodology has also demonstrated potential feasibility for scale-up with the successful production of 80 g in a single heat treatment.

4. Experimental Section

Preparation of NCA Precursor Mixture: The NCA precursor mixture was formed from two components that were freeze-dried together and gently ground by hand to ensure an intimate mixture. These components were a nanoprecipitate of the transition metal oxides/hydroxides and a batterygrade lithium hydroxide. The nanoprecipitate of the transition metal oxides/hydroxides was synthesized using a continuous hydrothermal flow synthesis (CHFS) reactor featuring a patented confined jet mixer (CJM, patent no WO2011148121A1). [25] The CHFS process has been described at lab and pilot plant scales elsewhere in the literature by some of the authors. [26] Briefly, the process can be described as follows; two identical high-pressure pumps (Primeroyal K, Milton Roy, France) were used to deliver: (i) an aqueous solution containing a mixture of metals, typically nitrates ≤0.5 M (pump P2) and (ii) the aqueous KOH base feed (pump P3), respectively. Both solutions were delivered at ambient temperature at 200 mL min⁻¹ and premixed in flow in a dead volume tee piece mixer, prior to entering the CJM. A third pump (pump P1) was used to pump room temperature DI water under pressure at 400 mL min⁻¹ into a heat exchanger at 450 °C. The combined P2 + P3 flow at ambient temperature was then mixed with superheated (supercritical) water in the CJM, whereupon precipitation and crystallization occurred (mixing temperature of \approx 333 °C). [27-29] Thereafter, the slurry was cooled in process after passing through a heat exchanger, and the coprecipitate aqueous slurry was collected at the exit of the CHFS process at \approx 50 °C. The collected slurry was then cleaned up using the following process: each slurry was centrifuged (model Sigma 6-16S, Sigma Aldrich, Dorset, UK) for 2 min at 4000 rpm, and the obtained wet solids were cleaned by dialysis over 1 week until the water conductivity was $<100 \mu S$. The cleaned slurry was then centrifuged for 3 h at 4000 rpm into a thick paste that was frozen and then freeze-dried at 3×10^{-7} MPa for 20 h (Virtis Genesis 35XL, Biopharma process systems, Winchester, UK) to obtain a free-flowing powder. The freeze-dried CHFS powder was then mixed with the appropriate amount of batterygrade lithium hydroxide monohydrate (LiOH·H2O) using the incipient wetness method and using a high-shear mixer (IKA, T18 digital package S2, Ultra-turrax) for 10 min. at 12 000 rpm followed by 16 000 rpm for 10 min. This resulting material was transferred to a stainless-steel tray, frozen, and then freeze-dried to obtain the final NCA precursor mixture. If the components are not well mixed by the above route, the subsequent efficient solid-state reactions are not achieved.



FHQ Treatment of the NCA Precursor Mixture: A preweighed amount of NCA precursor mixture was placed into an alumina boat and introduced into the center of a preheated 7.5 cm diameter and 105 cm long tube furnace (Elite TSHH split tube furnace, Market Harborough, UK), at a desired temperature, over the course of ≈1 min to avoid thermal shock. After a set amount of time, the sample was then removed over the space of another minute and then allowed to cool to room temperature. ^[30] The FHQ process was then repeated for a different time or temperature until all the samples had been obtained. A similar process was adopted for the larger-scale heat treatment (80 g total) using 10 by 6 cm alumina crucibles (Almath Crucibles), introducing them into a preheated muffle furnace.

Electrochemical Cell Preparation and Characterization: Electrodes were prepared by mixing the active material (NCA) with binder (poly-vinylidene fluoride, PVDF, PI-KEM, Staffordshire, UK) and conductive carbon black (Super P, Alfa Aesar, Heysham, UK) in a ratio of 80:10:10 wt%. A 10 wt% solution of PVDF in N-Methyl-2-pyrrolidone, NMP (Sigma Aldrich, Dorset, UK) was prepared using a magnetic stirrer and then mixed by hand with the conductive carbon and the active material. Further NMP (2.5 mL) was added to give a viscous slurry. The slurry was ball-milled at 800 rpm for 1 h before being cast on 15 μm thick aluminum foil (PI-KEM, Staffordshire, UK). The electrode sheets were dried on a hotplate at ≈150 °C for 20 min. The commercial NCA powder and preprinted sheets were obtained from Targray (Kirkland, QC, Canada).

All half-cell testing of the NCA materials was performed in CR2032 coin cells at room temperature on a Gamry Instruments Interface 1000 Galvanostat/Potentiostat (SciMed, Cheshire, UK). All cells were assembled in an Ar-filled glovebox with O_2 and $H_2O<0.5$ ppm. GF/B glass microfiber filters (Whatman, Buckinghamshire, UK) were used as separators and drenched in an electrolyte of 1M LiPF₆ in 1:1 wt% ethylene carbonate/diethyl methyl carbonate (BASF, Ludwigshafen, Germany). Lithium metal foil 15.6 mm diameter, 0.45 mm thick (PI-KEM, Staffordshire, UK) was used as a counter electrode.

Structural Characterization (PXRD, NPD, and PDF): PXRD patterns were collected using a STOE Stadi P diffractometer in transmission geometry (Mo-K α_1 radiation, λ = 0.70932 Å), equipped with a germanium (111) monochromator and a DECTRIS Mythen 1 k silicon strip detector (DECTRIS, Baden, Switzerland). A Yttria (Y $_2$ O $_3$) standard was used to estimate instrumental peak broadening. Datasets were collected over the 20 range of 2–40° with a step size of 0.5° and a count time of 5 s per step.

NPD was carried out on the NOMAD diffractometer at Oak Ridge National Laboratory. Each as-synthesized powder sample ($\approx\!2.5\,\mathrm{g}$) was placed into a vanadium cell. In this study, a wide d-spacing (0.11 < d < 5.29 Å) and a high resolution ($\Delta d/d=0.16\%$) were used for the NPD measurements. The sample environment was evacuated to prevent incoherent scattering of water vapor (H atoms). All experiments were measured for 4 h at room temperature. The neutron diffraction data were analyzed by Rietveld refinement using the GSAS-II software package, and PDF data were extracted using PDFgetN3 and analyzed using PDFgui software. $^{[31,32]}$ A value of 0.1 to 50 Å $^{-1}$ was used for $Q_{\rm min}$ and $Q_{\rm max}$ respectively, in the Fourier transform, and fitting was performed between 0.5 to 30 Å $^{-1}$.

SEM: SEM was performed using a JEOL JSM-6700 F microscope. To minimize charging, samples were deposited on copper foil tape, mounted on aluminum stubs, after dispersion in methanol (99.9%, Sigma Aldrich, Dorset, UK) and ultrasonication in a XUBA3 Ultrasonic Bath (Grant Instruments, Cambridge, UK) for 5 min. Image analysis was carried out using Image] software.

XAS (XANES and EXAFS): Ni K-edge and Co-K edge absorption measurements were performed at the B18 beamline of the Diamond synchrotron, Harwell, UK. The synchrotron radiation emitted by the bending magnet source was monochromated using a double crystal Si(111) monochromator. The data were collected in the transmission mode using three ionization chambers mounted in a series for simultaneous measurements on the sample and a metal foil reference. XANES data were extracted and normalized using the Athena software package, and Fourier transforms were performed with the Artemis software package to extract the EXAFS data.

Supporting Information

Supporting Information is available from the Wiley Online Library or from the author.

Acknowledgements

T.E.A. and J.A.D. would like the Faraday Institution for funding a 1-year Faraday Seed Project "Scale-up manufacturing of next generation ultrahigh-power Li-ion cathodes". J.W., Y.X., and J.A.D. would additionally like to thank the UKRI and the Faraday Institution for funding the CATMAT project. M.J.J. and A.J.E.R. acknowledge HORIBA-Motor Industry Research Association (MIRA), University College London (UCL), and the Engineering and Physical Sciences Research Council (EPSRC) (EP/R513143/1) for a Collaborative Awards in Science and Engineering (CASE) studentship.

Conflict of Interest

The authors declare no conflict of interest.

Data Availability Statement

The data that support the findings of this study are available from the corresponding author upon reasonable request.

Keywords

battery, cathode, flash synthesis, LiNi_xCo_vAl_zO₂, neutron

Received: April 16, 2025 Revised: July 25, 2025 Published online: 26999412, 0, Downloaded from https://advanced.onlinelibrary.wiley.com/doi/10.1002/aesr.202500149 by NICE, National Institute for Health and Care Excellence, Wiley Online Library on [23/99/2025]. See the Terms and Conditions (https://onlinelibrary.wiley

and-conditions) on Wiley Online Library for rules of use; OA articles are governed by the applicable Creative Commons

- [1] W. Li, E. M. Erickson, A. Manthiram, Nat. Energy 2020, 5, 26.
- [2] F. A. Susai, A. Bano, S. Maiti, J. Grinblat, A. Chakraborty, H. Sclar, T. Kravchuk, A. Kondrakov, M. Tkachev, M. Talianker, D. T. Major, B. Markovsky, D. Aurbach, J. Mater. Chem. A Mater. 2023, 11, 12958.
- [3] D. S. Ko, J. H. Park, B. Y. Yu, D. Ahn, K. Kim, H. N. Han, W. S. Jeon,
 C. Jung, A. Manthiram, Adv. Energy Mater. 2020, 10, 2001035.
- [4] K. Hoang, M. D. Johannes, J. Mater. Chem. A Mater. 2014, 2, 5224.
- [5] L. Yin, Z. Li, G. S. Mattei, J. Zheng, W. Zhao, F. Omenya, C. Fang, W. Li, J. Li, Q. Xie, E. M. Erickson, J. G. Zhang, M. S. Whittingham, Y. S. Meng, A. Manthiram, P. G. Khalifah, *Chem. Mater.* 2020, 32, 1002
- [6] G. H. Waller, A. Mansour, ECS Meeting Abstracts 2017, MA2017-02, https://doi.org/10.1149/ma2017-02/1/102.
- [7] D. Commandeur, C. Sabado, T. E. Ashton, J. A. Darr, J. Materiomics 2022, 8, 437.
- [8] Z. Ahaliabadeh, X. Kong, E. Fedorovskaya, T. Kallio, J. Power Sources 2022, 540, 231633.
- [9] S. Li, G. Qian, X. He, X. Huang, S. J. Lee, Z. Jiang, Y. Yang, W. N. Wang, D. Meng, C. Yu, J. S. Lee, Y. S. Chu, Z. F. Ma, P. Pianetta, J. Qiu, L. Li, K. Zhao, Y. Liu, Nat. Commun. 2022, 13, 704.
- [10] M. Malik, K. H. Chan, G. Azimi, Mater. Today Energy 2022, 28, 101066.
- [11] J. M. Price, P. Allan, P. Slater, Energy Adv. 2023, 2, 864.
- [12] Z. Liu, J. Zhang, J. Luo, Z. Guo, H. Jiang, Z. Li, Y. Liu, Z. Song, R. Liu, W.-D. Liu, W. Hu, Y. Chen, *Nanomicro Lett* **2024**, *16*, 210.
- [13] H. Jiang, C. Zeng, W. Zhu, J. Luo, Z. Liu, J. Zhang, R. Liu, Y. Xu, Y. Chen, W. Hu, Nano Res. 2024, 17, 2671.

on [23/09/2025]

. See the Terms

Wiley Online Library for rules of use; OA

governed by the applicable Creative Commons

ADVANCED
ENERGY & SUSTAINABILITY
RESEARCH

www.advenergysustres.com

- [14] R. Yin, Z. Guo, R. Liu, X.-S. Tao, Chin. Chem. Lett. 2025, 36, 109643.
- [15] N. V. Kosova, E. T. Devyatkina, V. V. Kaichev, J. Power Sources 2007, 174, 965.
- [16] X. Zhang, W. J. Jiang, A. Mauger, Qilu, F. Gendron, C. M. Julien, J. Power Sources 2010, 195, 1292.
- [17] T. E. Ashton, P. J. Baker, C. Sotelo-Vazquez, C. J. M. Footer, K. M. Kojima, T. Matsukawa, T. Kamiyama, J. A. Darr, J. Mater. Chem. A Mater 2021, 9, 10477.
- [18] T. Wang, K. Ren, W. Xiao, W. Dong, H. Qiao, A. Duan, H. Pan, Y. Yang, H. Wang, J. Phys. Chem. C 2020, 124, 5600.
- [19] T. Ohnuma, T. Kobayashi, RSC Adv. 2019, 9, 35655.
- [20] B. Philippe, M. Hahlin, K. Edström, T. Gustafsson, H. Siegbahn, H. Rensmo, J Electrochem. Soc. 2016, 163, A178.
- [21] F. Zhang, X. Zhou, X. Fu, C. Wang, B. Wang, W. Liang, P. Wang, J. Huang, S. Li, Mater. Today Energy 2021, 22, 100873.
- [22] M. M. Loghavi, H. Mohammadi-Manesh, R. Eqra, J. Solid State Electrochem. 2019, 23, 2569.
- [23] I. Hwang, C. W. Lee, J. C. Kim, S. Yoon, Mater. Res. Bull. 2012, 47, 73.

- [24] J. A. Darr, J. Zhang, N. M. Makwana, X. Weng, Chem. Rev. 2017, 117, 11125.
- [25] J. Darr, C. J. Tighe, R. Gruar, WO2011148121A1 2010.
- [26] J. A. Darr, J. Zhang, N. M. Makwana, X. Weng, Chem. Rev. 2017, 117, 11125
- [27] L. Hu, I. D. Johnson, S. Kim, G. M. Nolis, J. W. Freeland, H. D. Yoo, T. T. Fister, L. McCafferty, T. E. Ashton, J. A. Darr, J. Cabana, Nanoscale 2019, 11, 639.
- [28] D. Bauer, T. E. Ashton, A. R. Groves, A. Dey, S. Krishnamurthy, N. Matsumi, J. A. Darr, Energy Technol. 2020, 8, 1900692.
- [29] I. D. Johnson, T. E. Ashton, E. Blagovidova, G. J. Smales, M. Lübke, P. J. Baker, S. A. Corr, J. A. Darr, Sci. Rep. 2018, 8, 4114.
- [30] T. Ashton, J. Darr, S. Wang, WO2023233144A1 2023.
- [31] P. Juhás, J. N. Louwen, L. van Eijck, E. T. C. Vogt, S. J. L. Billinge, J. Appl. Crystallogr. 2018, 51, 1492.
- [32] C. L. Farrow, P. Juhas, J. W. Liu, D. Bryndin, E. S. Boin, J. Bloch, T. Proffen, S. J. L. Billinge, J. Phys. Condens. Matter 2007, 19, 335219.